

# Femtosecond currents in transition metal dichalcogenides monolayers

S. Azar Oliaei Motlagh, Vadym Apalkov, and Mark I. Stockman  
*Center for Nano-Optics (CeNO) and Department of Physics and Astronomy,  
 Georgia State University, Atlanta, Georgia 30303, USA*

(Dated: January 28, 2022)

We theoretically study the interaction of an ultrafast intense linearly polarized optical pulse with monolayers of transition metal dichalcogenides (TMDCs). Such a strong pulse redistributes electrons between the bands and generates femtosecond currents during the pulse. Due to the large bandwidth of the incident pulse, this process is completely off-resonant. While in TMDCs the time-reversal symmetry is conserved, the inversion symmetry is broken and these monolayers have the axial symmetry along armchair direction but not along the zigzag one. Therefore, the pulse polarized along the asymmetric direction of TMDC monolayer generates both longitudinal, i.e., along the direction of polarization, and transverse, i.e., in the perpendicular direction, currents. Such currents result in charge transfer through the system. We study different TMDC materials and show how the femtosecond transport in TMDC monolayers depend on their parameters, such as lattice constant and bandgap.

## I. INTRODUCTION

Nowadays, the femtosecond and strong field driven phenomena, e.g., high harmonic generations, the ultrafast ionization and metalization, the nonlinear current generations, and the nonlinear optical absorption in solids attract growing interest due to their possible applications in ultrafast optical switches, optoelectronic devices and ultimately in ultrafast information processing<sup>1–28</sup>. Among solids, transition metal dichalcogenides (TMDC) have unique optical and electrical properties. The bulk TMDCs are stacks of monolayers, which are bounded by the van der Waals forces<sup>29,30</sup>. Due to natural weakness of these forces, the bulk can be easily exfoliated to atomically thin monolayers<sup>30,31</sup>. Each monolayer is made of one layer of transition metal atoms like Mo and W, which is sandwiched between two chalcogen (S, Se, Te) layers. The monolayers can be found in different phases, while the semiconducting phase is the most common one. It has trigonal prismatic crystalline structures with  $D_{3h}$  point symmetry group<sup>32</sup>.

The TMDC monolayers are direct bandgap semiconductors with the bandgaps of 1.1–2.1 eV<sup>32</sup>. Similar to graphene, TMDC monolayers have honeycomb crystal structure but they are not centrosymmetric and the inversion symmetry is broken. Due to the broken inversion symmetry, the Berry curvature is not singular but has finite values with opposite signs in two valleys,  $K$  and  $K'$ . The finite Berry curvature gives rise to an anomalous Hall effect in the absence of external magnetic field<sup>33</sup>. Another difference of these materials from graphene is the existence of strong intrinsic spin orbit coupling<sup>32</sup>, which results in the spin splitting of the valence band (VB) and the conduction band (CB)<sup>32</sup> and makes TMDC monolayers suitable for spintronic applications.

Previously, we have shown that a single cycle of a circularly polarized optical pulse induces a large valley polarization,  $\eta_v \geq 40\% - 60\%$ , in TMDC monolayers,  $\text{MoS}_2$  and  $\text{WS}_2$ <sup>19</sup>. The mechanism of producing fundamentally fastest valley polarization in these monolayers is indepen-

dent of electron spin and has topological origin. Predominant population of one of the valleys in TMDC monolayer is not due to the optical selection rule as in case of a continuous wave but due to topological resonance, which is a competition of the dynamic phase and the topological phase that is accumulated during ultrashort and strong pulse<sup>19</sup>. It has been also recently predicted that the valley polarization can be tuned by the bandgap in gapped graphene monolayers<sup>34</sup>. In graphene, the inversion symmetry can be broken by placing graphene on different substrates, e.g., SiC, which reduces the point group symmetry of graphene from  $D_{6h}$  to  $D_{3h}$ <sup>35,36</sup>.

In the field of intense optical pulse the valence and conduction band states are strongly coupled, which results in generation of strong nonlinear electric currents and finite transfer of electric charge through the system. Thus ultrafast optical pulses allow to control the transport properties of electron systems and enhance the conductivity of solids on the femtosecond time scale. Understanding of the extent of such control is important for possible device application of different solids. In this article we study the femtosecond currents driven by a single-cycle of an intensive laser pulse in monolayers of different TMDC materials. Different characteristics, e.g., the energy dispersion and the lattice constants, of these materials strongly affect the generated electric current and correspondingly transferred charge. The generated electric current also depends on the direction of polarization of the optical pulse<sup>37</sup>.

## II. MAIN EQUATIONS

We consider coherent ultrafast electron dynamics in the field of the pulse, assuming that the relaxation and scattering times in TMDC monolayers are longer than 10 fs<sup>38–42</sup>. The time dependent Hamiltonian of the system has the following form

$$H(t) = H_0 - e\mathbf{r}\mathbf{F}(t), \quad (1)$$

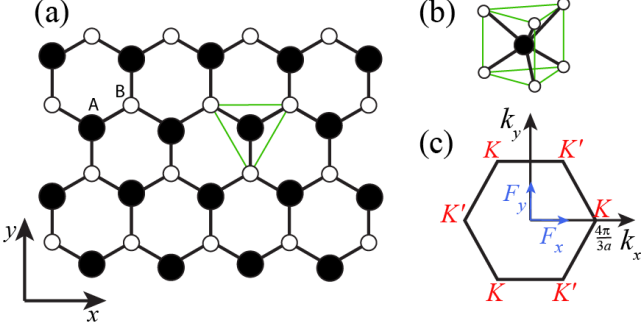


FIG. 1. (Color online) Crystal structure of TMDC monolayer. (a,b) Honeycomb crystal structure of TMDC monolayer consists of two sublattices:  $A$  and  $B$ . Sublattice  $A$  is occupied by transition metal atoms (closed dots), while sublattice  $B$  is occupied by chalcogen atoms (open dots). (c) The first Brillouin zone with two valleys,  $K$  and  $K'$ . For general polarization of the optical pulse, the electric field in the pulse has both  $x$  and  $y$  components,  $F_x$  and  $F_y$ .

where  $H_0$  is the field-free Hamiltonian of a TMDC monolayer,  $e$  is an electron charge,  $\mathbf{r}$  is the position vector, and  $\mathbf{F}(t)$  is the electric field of the pulse. We consider the three-band tight binding model for TMDC monolayer, which gives three bands: one valence band and two conduction bands. For the pulse, linearly polarized in the  $x$ -direction, the electric field is given by the following expression

$$F_x(t) = F_0(1 - 2u^2)e^{-u^2}, \quad F_y(t) = 0, \quad (2)$$

where  $u = t/\tau$ , and  $\tau = 1$  fs is the pulse duration.

The electron dynamics is determined by the solution of the corresponding time dependent Schrodinger equation (TDSE)

$$i\hbar \frac{d\Psi(t)}{dt} = H(t)\Psi(t). \quad (3)$$

It is convenient to express this solution in the basis of time dependent Houston functions<sup>43</sup>

$$\Phi_{\alpha\mathbf{q}}^{(H)}(\mathbf{r}, t) = \Psi_{\mathbf{k}(\mathbf{q}, t)}^{(\alpha)}(\mathbf{r}) \exp(i\phi_{\alpha}^{(D)}(q, t) + i\phi_{\alpha}^{(B)}(q, t)), \quad (4)$$

where  $\Psi_{\mathbf{k}}^{(\alpha)}(\mathbf{r})$  are the eigenfunctions of the time independent part of Hamiltonian  $H_0$  and  $\phi_{\alpha}^{(D)}(q, t) = -\frac{1}{\hbar} \int dt' E_{\alpha}[\mathbf{k}(\mathbf{q}, t')]$  is the dynamic phase,  $E_{\alpha}$  are the eigenvalues of  $H_0$ ,  $\phi_{\alpha}^{(B)}(q, t) = -\frac{e}{\hbar} \int dt' \mathbf{F}(t') \mathbf{A}_{\alpha\alpha}[\mathbf{k}(\mathbf{q}, t')]$  is the Berry phase,  $\mathbf{A}_{\alpha\alpha}$  is the Berry connection, which is defined below by Eq. (14), and  $\alpha \in \{v, c_1, c_2\}$  where  $v, c_1, c_2$  denote the VB and two CBs, respectively. The electron trajectory in the reciprocal space,  $\mathbf{k}(\mathbf{q}, t)$ , is given by the Bloch acceleration theorem<sup>44</sup>,

$$\mathbf{k}(\mathbf{q}, t) = \mathbf{q} + \frac{e}{\hbar} \int_{-\infty}^t \mathbf{F}(t') dt' \quad (5)$$

where  $\mathbf{q}$  is the initial crystal wave vector.

In the basis of Houston functions, solutions of the time dependent Schrodinger equation (3) are parameterized by initial crystal wave vector  $\mathbf{q}$  and are given by the following expression

$$\Psi_{\mathbf{q}}(\mathbf{r}, t) = \sum_{\alpha=c_1, c_2, v} \beta_{\alpha\mathbf{q}}(t) \Phi_{\alpha\mathbf{q}}^{(H)}(\mathbf{r}, t), \quad (6)$$

where  $\beta_{\alpha\mathbf{q}}(t)$  are expansion coefficients, which satisfy the following system of differential equations

$$i\hbar \frac{\partial B_{\mathbf{q}}(t)}{\partial t} = H'(\mathbf{q}, t) B_{\mathbf{q}}(t). \quad (7)$$

Here

$$B_{\mathbf{q}}(t) = \begin{bmatrix} \beta_{c_2\mathbf{q}}(t) \\ \beta_{c_1\mathbf{q}}(t) \\ \beta_{v\mathbf{q}}(t) \end{bmatrix}, \quad (8)$$

$$H'(\mathbf{q}, t) = -e\mathbf{F}(t) \hat{\mathcal{A}}(\mathbf{q}, t), \quad (9)$$

$$\hat{\mathcal{A}}(\mathbf{q}, t) = \begin{bmatrix} 0 & \mathcal{D}_{c_2c_1}(\mathbf{q}, t) & \mathcal{D}_{c_2v}(\mathbf{q}, t) \\ \mathcal{D}_{c_2c_1}^*(\mathbf{q}, t) & 0 & \mathcal{D}_{c_1v}(\mathbf{q}, t) \\ \mathcal{D}_{c_2v}^*(\mathbf{q}, t) & \mathcal{D}_{c_1v}^*(\mathbf{q}, t) & 0 \end{bmatrix}. \quad (10)$$

where

$$\mathcal{D}_{\alpha\alpha_1}(\mathbf{q}, t) = \mathcal{A}_{\alpha\alpha_1}[\mathbf{k}(\mathbf{q}, t)] \times \exp\left(i\phi_{\alpha\alpha_1}^{(D)}(\mathbf{q}, t) + i\phi_{\alpha\alpha_1}^{(B)}(\mathbf{q}, t)\right), \quad (11)$$

$$\phi_{\alpha\alpha_1}^{(D)}(\mathbf{q}, t) = \phi_{\alpha_1}^{(D)}(\mathbf{q}, t) - \phi_{\alpha}^{(D)}(\mathbf{q}, t), \quad (12)$$

$$\phi_{\alpha\alpha_1}^{(B)}(\mathbf{q}, t) = \phi_{\alpha_1}^{(B)}(\mathbf{q}, t) - \phi_{\alpha}^{(B)}(\mathbf{q}, t), \quad (13)$$

$$\mathcal{D}_{\alpha\alpha_1} = e\mathcal{A}_{\alpha\alpha_1}; \quad \mathcal{A}_{\alpha\alpha_1}(\mathbf{q}) = \left\langle \Psi_{\mathbf{q}}^{(\alpha)} \left| i \frac{\partial}{\partial \mathbf{q}} \right| \Psi_{\mathbf{q}}^{(\alpha_1)} \right\rangle. \quad (14)$$

Here,  $\mathcal{A}_{\alpha\alpha_1}(\mathbf{k})$  is non-Abelian Berry connection<sup>45–47</sup>, and  $\mathcal{D}_{\alpha\alpha_1}$  is the interband dipole matrix, which determines the optical transitions between the VB and CBs.

The crystal structure of TMDC monolayer is shown in Fig. 1. It has  $D_{3h}$  symmetry and consists of two sublattices  $A$  and  $B$ , which are occupied by transition metal atoms (sublattice  $A$ ) and chalcogen atoms (sublattice  $B$ ). The first Brillouin zone of TMDC monolayer is a hexagon with two valleys,  $K$  and  $K'$  - see Fig. 1(c). We describe TMDC monolayer within the three band tight binding model<sup>32</sup>. In this model only the couplings between the nearest neighbor  $d$  orbitals ( $d_{xy}$ ,  $d_{z^2}$ , and  $d_{x^2-y^2}$ ) of transition metal atoms are considered. The corresponding Hamiltonian is the sum of the nearest neighbor tight-binding Hamiltonian  $H^{(\text{TNN})}$ , and spin orbit coupling (SOC) contribution  $H^{(\text{SOC})}$ <sup>32</sup>,

$$\begin{aligned} H_0(\mathbf{k}) &= I \otimes H^{(\text{TNN})} + H^{(\text{SOC})} \\ &= \begin{bmatrix} H^{(\text{TNN})}(\mathbf{k}) + \frac{\lambda}{2} L_z & 0 \\ 0 & H^{(\text{TNN})}(\mathbf{k}) - \frac{\lambda}{2} L_z \end{bmatrix} \\ &= \begin{bmatrix} H_{3 \times 3}^{\uparrow}(\mathbf{k}) & 0 \\ 0 & H_{3 \times 3}^{\downarrow}(\mathbf{k}) \end{bmatrix}, \end{aligned} \quad (15)$$

	MoS <sub>2</sub>	WS <sub>2</sub>	MoSe <sub>2</sub>	WSe <sub>2</sub>	MoTe <sub>2</sub>	WTe <sub>2</sub>
a (Å)	3.19	3.191	3.326	3.325	3.557	3.560
λ (eV)	0.073	0.211	0.091	0.228	0.107	0.237
Δ <sub>K</sub> <sup>Up</sup> = Δ <sub>K'</sub> <sup>Down</sup> (eV)	1.590	1.600	1.346	1.325	0.967	0.835
Δ <sub>K</sub> <sup>Down</sup> = Δ <sub>K'</sub> <sup>Up</sup> (eV)	1.736	2.023	1.526	1.776	1.180	1.307

TABLE I. Lattice constant, spin orbit coupling constant, and bandgap (for spin up and spin down) at the  $K$  and  $K'$  points for different TMDC monolayers<sup>32</sup>.

where the tight binding matrix  $H^{(\text{TNN})}$  is given in Appendix A,  $\lambda$  is the SOC constant<sup>32</sup>, and

$$L_z = \begin{bmatrix} 0 & 0 & 0 \\ 0 & 0 & 2i \\ 0 & -2i & 0 \end{bmatrix}. \quad (16)$$

Since, the two spin components are not coupled by external electric field, we solve TDSE for each spin component independently.

The main parameters of TMDC monolayers, which are the bandgap, lattice constant, and SOC constant, are shown in Table I. The lattice constant is in the range of 3.19 – 3.56 Å, while the bandgap lies between 0.8 eV and 2.0 eV.

The femtosecond field-driven currents in solids generally have two main contributions, which come from interband and intraband dynamics. While these contributions are not gauge invariant quantities, the total current, which is the sum of two contributions, is gauge invariant<sup>48</sup>. We use the following expressions to calculate the intraband,  $\mathbf{J}_{\text{ra}}$ , and interband,  $\mathbf{J}_{\text{er}}$ , currents,

$$\mathbf{J}_{\text{ra}}(t) = \frac{e}{a^2} \sum_{g_s} \sum_{\alpha=v, c_1, c_2, \mathbf{q}} |\beta_{\alpha, g_s}(\mathbf{q}, t)|^2 \mathbf{v}_{\alpha, g_s}(\mathbf{k}(\mathbf{q}, t)), \quad (17)$$

where  $\mathbf{v}_{\alpha, g_s}(\mathbf{k}) = \frac{\partial}{\partial \mathbf{k}} E_{\alpha, g_s}(\mathbf{k})$  is the group velocity (intra-band velocity) and  $g_s$  is the electron spin; the interband current is given by the following expression

$$\begin{aligned} \mathbf{J}_{\text{er}}(t) = & i \frac{e}{\hbar a^2} \sum_{g_s} \sum_{\substack{\alpha, \alpha' = v, c_1, c_2 \\ \alpha \neq \alpha'}} \beta_{\alpha', g_s}^*(\mathbf{q}, t) \beta_{\alpha, g_s}(\mathbf{q}, t) \\ & \times \exp\{i\phi_{\alpha', g_s}^{(\text{D})}(\mathbf{q}, t) + i\phi_{\alpha, g_s}^{(\text{B})}(\mathbf{q}, t)\} \\ & \times [E_{\alpha', g_s}(\mathbf{k}(\mathbf{q}, t)) - E_{\alpha, g_s}(\mathbf{k}(\mathbf{q}, t))] \mathcal{A}_{\alpha', g_s}(\mathbf{k}(\mathbf{q}, t)). \end{aligned} \quad (18)$$

### III. RESULTS AND DISCUSSION

Below we consider the following TMDC materials: MoS<sub>2</sub>, WS<sub>2</sub>, MoSe<sub>2</sub>, WSe<sub>2</sub>, MoTe<sub>2</sub>, and WTe<sub>2</sub>. The parameters for these materials are taken from Ref.<sup>32</sup>. The

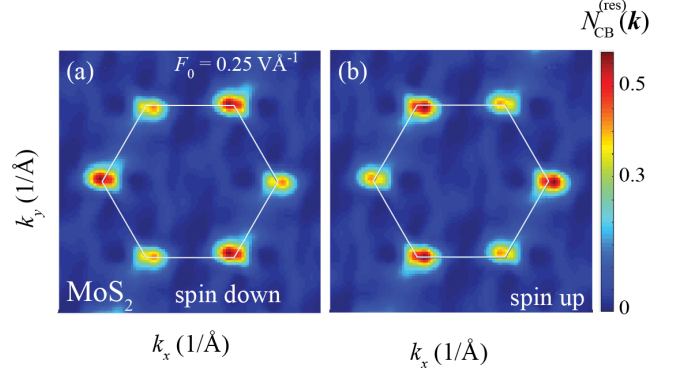


FIG. 2. (Color online) Residual CB population distribution in the reciprocal space. The distribution is shown for MoS<sub>2</sub> monolayer and for (a) spin down and (b) spin up components. The white solid lines show the boundary of the first Brillouin zone. The pulse is polarized in the  $x$  direction.

crystal structure of the corresponding TMDC monolayer with the first Brillouin zone is shown Fig. 1. Within the three band tight binding model the monolayer has one valence band (VB) and two conduction bands (CBs). Initially, i.e., before the pulse, the valence band is occupied and the conduction bands are empty. We apply a linearly polarized pulse propagating along  $z$  direction with the amplitude of  $\sim 0.1 - 0.5 \text{ VÅ}^{-1}$  and the duration of  $\sim 5 \text{ fs}$ .

One the characteristics of electron dynamics in the field of the pulse is CB population distribution in the reciprocal space,  $N_{\text{CB}}(\mathbf{k}) = |\beta_{\text{C1}, \mathbf{k}}|^2 + |\beta_{\text{C2}, \mathbf{k}}|^2$ . Such distribution is nonzero during the pulse and its residual value,  $N_{\text{CB}}^{(\text{res})}(\mathbf{k})$ , determines irreversibility of the electron dynamics. As theoretical and experimental studies show the ultrafast electron dynamics is irreversible in semimetals, e.g. graphene<sup>13,49</sup>, Weyl semimetals<sup>50</sup> and semiconductors, black phosphorene<sup>51</sup>, and TMDCs monolayers<sup>19,52</sup>. In addition to the irreversibility, the residual CB population distribution,  $N_{\text{CB}}^{(\text{res})}(\mathbf{k})$ , also determines the valley polarization after a circularly polarized pulse<sup>19</sup>.

Typical for TMDC monolayers, the residual CB population distribution in the reciprocal space is shown in Fig. 2 for two spin components, down (a) and up (b). The pulse is linearly polarized in  $x$ -direction with the amplitude of  $0.25 \text{ VÅ}^{-1}$ . The CB population is large near the  $K$  and  $K'$  valleys, which is due to large interband coupling at these two points. For such small field amplitude, the population distribution does not show any interference fringes. For a given spin component, up or down, one valley is more populated than another one. For example, for spin down (see Fig. 2(a)), the CB population of  $K'$  valley is higher than the corresponding population of the  $K$  valley. However, the total CB population, summed over both spin components, is the same for both valleys. This is because the linear polarized pulse preserves the

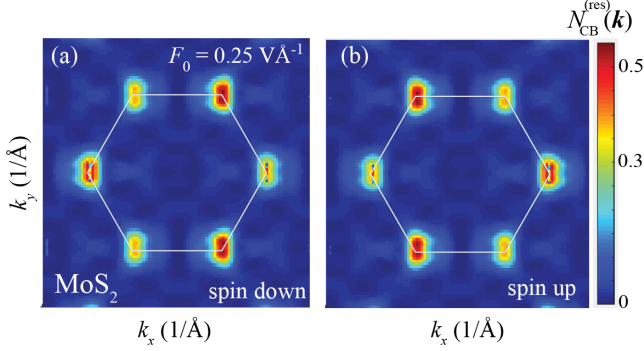


FIG. 3. (Color online) The same as Fig. 2 but for the pulse polarized in the  $y$  direction.

time reversal symmetry and does not induce any valley polarization. The axis  $x$  is not the axis of symmetry of TMDC monolayer and the residual CB population distribution, shown in Fig. 2, clearly shows such asymmetry. Because the CB population distribution is not symmetric with respect to the  $x$  axis, the electric current is generated in both  $x$  and  $y$  directions.

The CB population distribution for the applied pulse polarized in  $y$  direction is shown in Fig. 3. Similar to the  $x$  polarized pulse, the CB population is concentrated near the  $K$  and  $K'$  valleys with zero residual valley polarization. The  $y$  axis is the axis of symmetry of the system and the CB population distribution is symmetric with respect to the  $y$  axis. Because of this symmetry, the electric current is generated during the pulse only in  $y$  direction.

The ultrafast field driven intraband and interband electron dynamics generates an electric current. For the pulse polarized in  $x$  direction, i.e., along the zigzag direction, the electric current is generated in both  $x$  and  $y$  directions<sup>37</sup>. The current along  $y$  direction, i.e., the direction perpendicular to the polarization of the pulse, strongly depends on the bandgap of TMDC monolayer. It disappears at zero bandgap, e.g., for pristine graphene, when the  $x$  axis is the axis of symmetry. For the pulse polarized in  $y$  axis, which is the axis of symmetry of TMDC monolayer, the electric current is generated only along the direction of polarization of the pulse. Below we consider only the electric pulse polarized in  $x$  direction, which covers electron transport both in the direction of the pulse polarization and in the perpendicular direction.

The generated electric currents for different TMDC materials are shown in Fig. 4. The pulse is polarized in the  $x$  direction so both  $J_x$  and  $J_y$  components of the current are nonzero. The field amplitude is  $0.25 \text{ V/\AA}$ . The  $x$  component of the current for all TMDC materials shows the same profile during the pulse, i.e.,  $-2fs < t < 2fs$ , but after the pulse,  $J_x$  has oscillatory behavior with the frequency of oscillations that depends on the bandgap of TMDC monolayer, which is in the range of  $0.8 - 2 \text{ eV}$  for the TMDC materials shown in the figure. Such oscil-

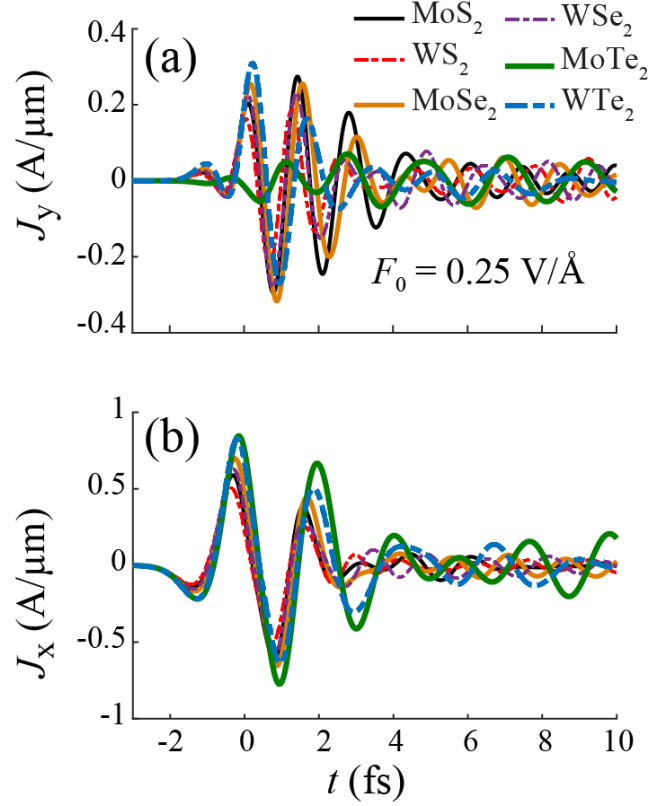


FIG. 4. (Color online) Femtosecond field driven currents as a function of time in different TMDC monolayers. The generated electric currents have both the  $y$  components (a) and the  $x$  components (b). The pulse is linearly polarized in the  $x$  direction and its amplitude is  $0.25 \text{ V/\AA}$ .

lations in the residual current  $J_x$  is due to the fact that the main contribution to the current is the interband one, while the intraband contribution, which depends only on the population of the conduction and valence bands and thus do not show oscillation after the pulse, is small.

The generated current in the  $y$  direction is almost three times smaller than the current in the  $x$  direction. It also shows the oscillatory behavior as a function of time with well pronounced bandgap-dependent oscillations after the pulse. Although the profile of current  $J_y$  during the pulse ( $-2fs < t < 2fs$ ) is almost the same for all TMDC monolayers, one TMDC material, namely  $\text{MoTe}_2$ , shows completely different time dependence.

The unique behavior of  $\text{MoTe}_2$  monolayer can be understood from the corresponding CB population distribution in the reciprocal space. The residual CB populations are shown in Fig. 5 for different TMDC monolayers. For all monolayers except  $\text{MoTe}_2$ ,  $N_{\text{CB}}^{(\text{res})}(\mathbf{k})$  is concentrated at the  $K$  and  $K'$  points along both  $k_x$  and  $k_y$  directions. As a result they all show the same time dependence of the generated current for both  $x$  and  $y$  directions. At the same time, for  $\text{MoTe}_2$  monolayer, the CB population distribution is completely different. While along the direc-

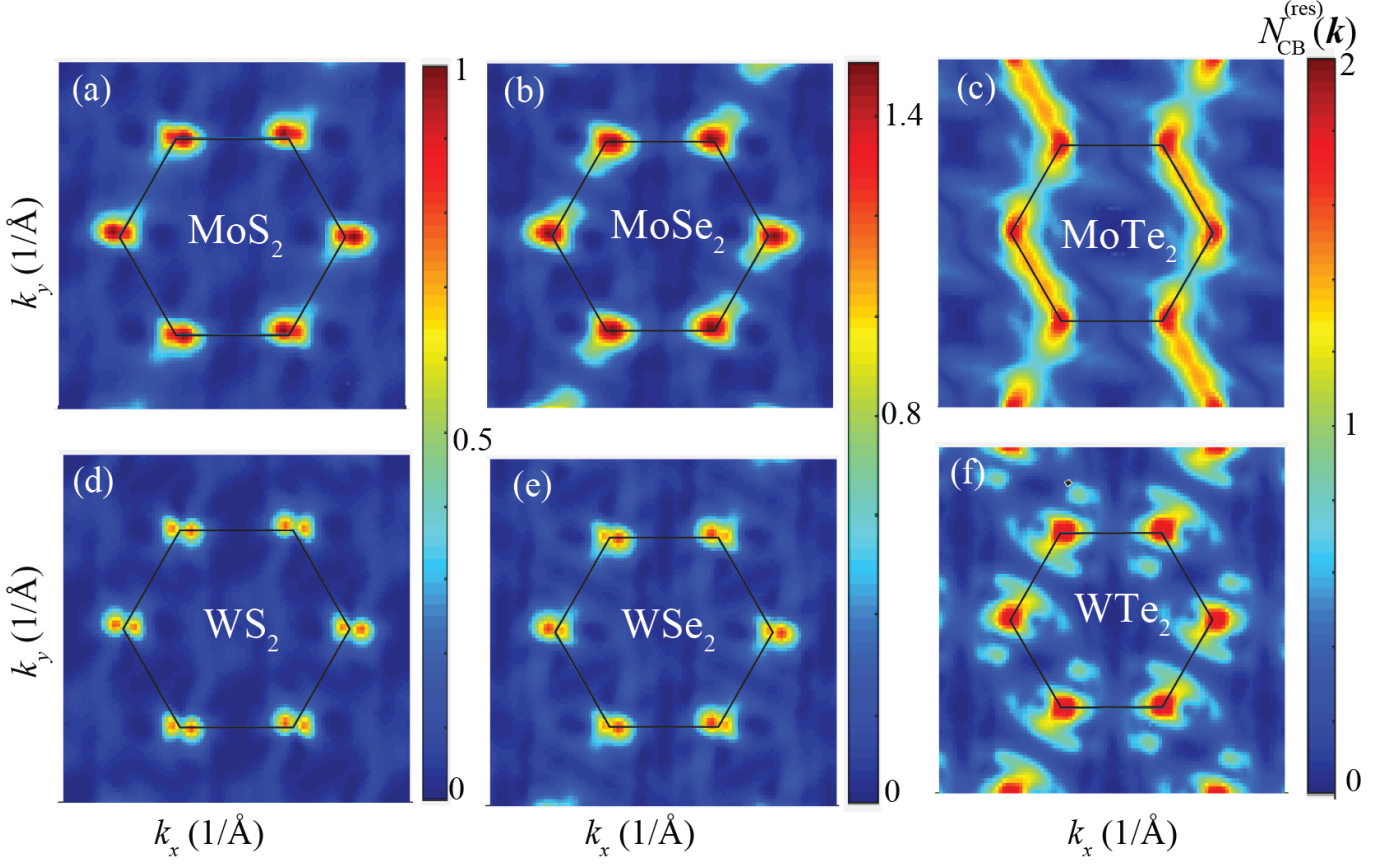


FIG. 5. (Color online) Residual CB population distributions in the reciprocal space for different TMDC monolayers: (a) MoS<sub>2</sub>, (b) MoSe<sub>2</sub>, (c) MoTe<sub>2</sub>, (d) WS<sub>2</sub>, (e) WSe<sub>2</sub>, and (f) WTe<sub>2</sub>. The optical pulse is linearly polarized in the  $x$  direction and its amplitude is  $0.25 \text{ V \AA}^{-1}$ . The black solid lines show the edges of the first Brillouin zone. For all TMDC monolayers, except MoTe<sub>2</sub>, the CB population is concentrated near the  $K$  and  $K'$  points.

tion of the pulse polarization, i.e.,  $x$  direction,  $N_{\text{CB}}^{(\text{res})}(\mathbf{k})$  is concentrated near the  $K$  and  $K'$  points, in the perpendicular direction, i.e.,  $y$  direction, it is highly delocalized and there is a large CB population along the lines connecting the  $K$  and  $K'$  points - see Fig. 5(c). Thus, along the  $x$  direction  $N_{\text{CB}}^{(\text{res})}(\mathbf{k})$  behaves similar for MoTe<sub>2</sub> and other TMDC materials and the corresponding current  $J_x$  shows similar time dependence for all TMDC monolayers. Along the  $y$  direction  $N_{\text{CB}}^{(\text{res})}(\mathbf{k})$  of MoTe<sub>2</sub> monolayer is much more extended compared to other TMDC monolayers, as a result the corresponding current,  $J_y$ , has completely different time dependence for MoTe<sub>2</sub> monolayer.

The dependence of the electric current on the field amplitude,  $F_0$ , is shown in Fig. 6 for MoS<sub>2</sub> monolayer. For other TMDC materials the dependence on  $F_0$  is similar. As expected, the generated current monotonically increases with  $F_0$ . In residual current, the frequency of oscillations, which is determined by the bandgap, does not depend on  $F_0$ .

One of the characteristics of nonlinearity of electron response to an ultrashort pulse is a transferred charge through the system during the pulse, which can be also

measured experimentally<sup>2,5</sup>. The transferred charge is defined by the following expression

$$\mathbf{Q} = \int_{-\infty}^{\infty} \mathbf{J}(t) dt'. \quad (19)$$

Since the residual current shows an oscillating behavior, to eliminate the dependence on the upper limit in the above integral we introduce a relaxation time of 5 fs when calculating the transferring charge. The transferred charge is also the residual polarization of the system.

The transferred charge as a function of the field amplitude,  $F_0$ , is shown in Fig. 7 for different TMDC monolayers. The transferred charge along the  $y$  direction,  $Q_y$ , monotonically increases with  $F_0$  - see Fig. 7(a). For all TMDC monolayers, except MoTe<sub>2</sub>, the charge is transferred in the positive direction of the  $y$  axis, while for MoTe<sub>2</sub> the transfer of the charge occurs in the negative direction of the  $y$  axis. Such direction of the transfer corresponds to the condition that the field maximum of the pulse is in the positive direction of the  $x$  axis. The magnitude of the transferred charge increases with decreasing the bandgap of TMDC monolayer. The largest charge



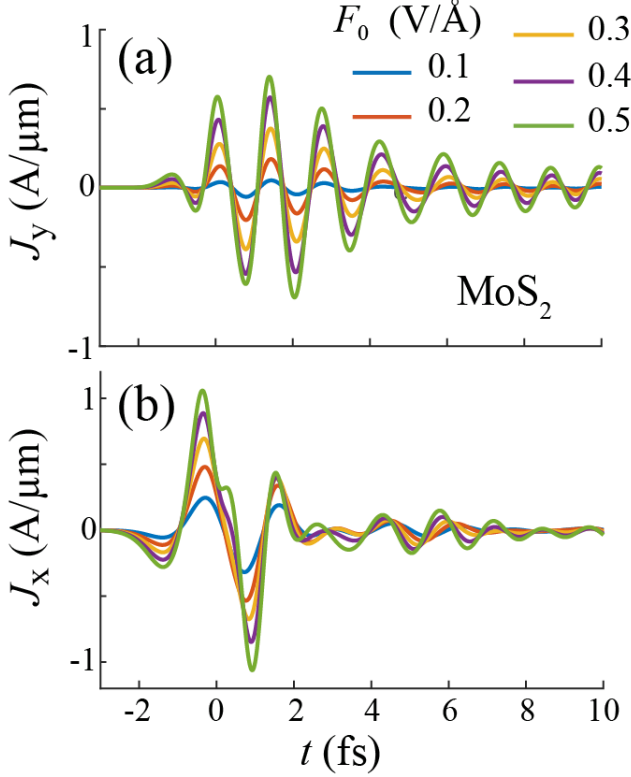


FIG. 6. (Color online) Ultrafast field driven currents in MoS<sub>2</sub> monolayer as a function of time for different field amplitudes. The  $y$  component (a) and the  $x$  component (b) of the current are shown. The optical pulse is linearly polarized in the  $x$  direction.

transfer occurs for WTe<sub>2</sub> monolayer, while the smallest - for MoTe<sub>2</sub> monolayer.

Along the  $x$  axis [see Fig. 7(b)], the charge is transferred in the direction of the field maximum for all TMDC monolayers. The dependence of  $Q_x$  on the pulse amplitude,  $F_0$ , is nonmonotonic. The transferred charge reaches its maximum at some value of  $F_0 = F_{max}$  and then decreases with  $F_0$ . The value of  $F_{max}$  is partially correlated with the condition that at this field an electron, which is initially at one valley, say valley  $K$ , reaches the second valley,  $K'$ , during the pulse. For example, for TMDC monolayers with large lattice constants, MoTe<sub>2</sub> : 3.557 Å and WTe<sub>2</sub> : 3.560 Å<sup>32</sup>, the maxima occur at lower field amplitudes. Although the lattice constant is not the only parameter, which determines  $Q_x$  dependence on  $F_0$ , the transferred charge also depends on the bandgap and spin orbit coupling of TMDC monolayer. In terms of applications, the data in Fig. 7(b) illustrate that MoTe<sub>2</sub> monolayer is the most sensitive to the pulse amplitude, i.e., for MoTe<sub>2</sub> monolayer, the transferred charge,  $Q_x$ , shows relatively sharp maximum with strong dependence on  $F_0$ .

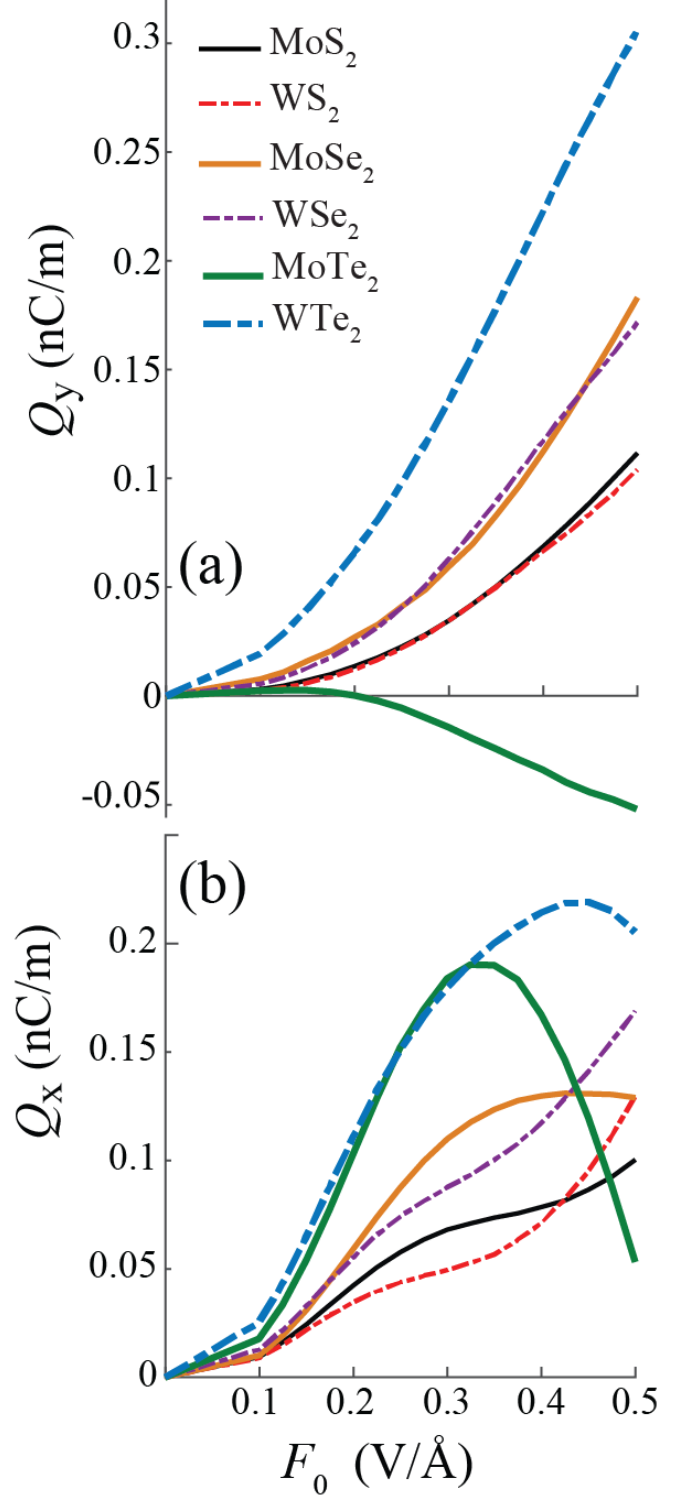


FIG. 7. (Color online) Charge transferred through the system during the pulse as a function of the field amplitude,  $F_0$ , for different TMDC monolayers. The transferred charge along the  $y$  direction (a) and the  $x$  direction (b) is shown. The optical pulse is linearly polarized in the  $x$  direction.

#### IV. CONCLUSION

The ultrafast field driven currents in solids are governed by interband and intraband electron dynamics, resulting in two contributions, intraband and interband, to the electric current. In TMDC monolayers, the generated electric current is mainly determined by the interband contribution. As a result, the residual current as a function of time shows oscillations, the frequency of which is determined by the bandgap of the corresponding TMDC monolayer. The TMDC monolayers have broken inversion symmetry, their symmetry group is  $D_{3h}$ , and they have only three axes of symmetry, which are along the armchair directions. If the optical pulse is polarized along the direction of symmetry of the monolayer then the electric current is generated only along the direction of polarization. But if the polarization of the optical pulse is along a non-symmetric direction, for example, along the zigzag direction, then the electric current is generated both along the direction of polarization and in the perpendicular direction.

For all TMDC monolayers the longitudinal electric current, i.e., the current along the direction of polarization of the pulse, show similar behavior as a function of time. Such current transfers an electric charge along the direction of the field maximum. As a function of the field amplitude, the transferred charge has a maximum, the position of which depends on the lattice constant of TMDC monolayer. MoTe<sub>2</sub> monolayer is the most sensitive to the parameters of the optical pulse.

The transverse current also results in the charge transfer through the system during the pulse. The magnitude of the transferred charge monotonically increases with the field amplitude, while the direction of the transfer depends on the TMDC material. Control of an electron transport on a femtosecond time scale pave the way for ultrafast electronic application of TMDCs monolayers.

#### Appendix A: Tight binding Hamiltonian

The three band nearest-neighbor (TNN) tight-binding Hamiltonian,  $H^{(\text{TNN})}$ , of TMDC monolayer is constructed from three orbitals ( $d_{z^2}$ ,  $d_{xy}$ , and  $d_{x^2-y^2}$ ) of transition metal atoms<sup>32</sup>. The Hamiltonian is given by the following expression

$$H^{\text{TNN}}(\mathbf{k}) = \begin{bmatrix} V_0 & V_1 & V_2 \\ V_1^* & V_{11} & V_{12} \\ V_2^* & V_{12}^* & V_{22} \end{bmatrix}, \quad (\text{A1})$$

where

$$\begin{aligned} V_0 &= \epsilon_1 + 2t_0(2 \cos \alpha \cos \beta + \cos 2\alpha) \\ &\quad + 2r_0(2 \cos 3\alpha \cos \beta + \cos 2\beta) \\ &\quad + 2u_0(2 \cos 2\alpha \cos 2\beta + \cos 4\alpha), \\ \text{Re}[V_1] &= -2\sqrt{3}t_2 \sin \alpha \sin \beta + 2(r_1 + r_2) \sin 3\alpha \sin \beta \\ &\quad - 2\sqrt{3}u_2 \sin 2\alpha \sin 2\beta, \\ \text{Im}[V_1] &= 2t_1 \sin \alpha(2 \cos \alpha + \cos \beta) \\ &\quad + 2(r_1 - r_2) \sin 3\alpha \cos \beta \\ &\quad + 2u_1 \sin 2\alpha(2 \cos 2\alpha + \cos 2\beta), \\ \text{Re}[V_2] &= 2t_2(\cos 2\alpha - \cos \alpha \cos \beta) \\ &\quad - \frac{2}{\sqrt{3}}(r_1 + r_2)(\cos 3\alpha \cos \beta - \cos 2\beta) \\ &\quad + 2u_2(\cos 4\alpha - \cos 2\alpha \cos 2\beta), \\ \text{Im}[V_2] &= 2\sqrt{3}t_1 \cos \alpha \sin \beta \\ &\quad + \frac{2}{\sqrt{3}} \sin \beta(r_1 - r_2)(\cos 3\alpha + 2 \cos \beta) \\ &\quad + 2\sqrt{3}u_1 \cos 2\alpha \sin 2\beta, \\ V_{11} &= \epsilon_2 + (t_{11} + 3t_{22}) \cos \alpha \cos \beta \\ &\quad + 2t_{11} \cos 2\alpha + 4r_{11} \cos 3\alpha \cos \beta \\ &\quad + 2(r_{11} + \sqrt{3}r_{12} \cos 2\beta) \\ &\quad + (u_{11} + 3u_{22}) \cos 2\alpha \cos 2\beta + 2u_{11} \cos 4\alpha, \\ \text{Re}[V_{12}] &= \sqrt{3}(t_{22} - t_{11}) \sin \alpha \sin \beta \\ &\quad + 4r_{12} \sin 3\alpha \sin \beta \\ &\quad + \sqrt{3}(u_{22} - u_{11} \sin 2\alpha \sin 2\beta), \\ \text{Im}[V_{12}] &= 4t_{12} \sin \alpha(\cos \alpha - \cos \beta) \\ &\quad + 4u_{12} \sin 2\alpha(\cos 2\alpha - \cos 2\beta), \\ V_{22} &= \epsilon_2 + (3t_{11} + t_{22}) \cos \alpha \cos \beta + 2t_{22} \cos 2\alpha \\ &\quad + 2r_{11}(2 \cos 3\alpha \cos \beta + \cos 2\beta) \\ &\quad + \frac{2}{\sqrt{3}}r_{12}(4 \cos 3\alpha \cos \beta - \cos 2\beta) \\ &\quad + (3u_{11} + u_{22}) \cos 2\alpha \cos 2\beta + 2u_{22} \cos 4\alpha, \end{aligned} \quad (\text{A2})$$

and

$$(\alpha, \beta) = \left( \frac{1}{2}k_x a, \frac{\sqrt{3}}{2}k_y a \right). \quad (\text{A3})$$

The values of the parameters in the above Hamiltonian for different TMDC materials are given in table II Ref [32].

#### ACKNOWLEDGMENTS

Major funding was provided by Grant No. DE-FG02-01ER15213 from the Chemical Sciences, Biosciences and Geosciences Division, Office of Basic Energy Sciences,

	MoS <sub>2</sub>	WS <sub>2</sub>	MoSe <sub>2</sub>	WSe <sub>2</sub>	MoTe <sub>2</sub>	WTe <sub>2</sub>
$a$	3.19	3.191	3.326	3.325	3.557	3.560
$\epsilon_1$	0.683	0.717	0.684	0.728	0.588	0.697
$\epsilon_2$	1.707	1.916	1.546	1.655	1.303	1.380
$t_0$	-0.146	-0.152	-0.146	-0.146	-0.226	-0.109
$t_1$	-0.114	-0.097	-0.130	-0.124	-0.234	-0.164
$t_2$	0.506	0.590	0.432	0.507	0.036	0.368
$t_{11}$	0.085	0.047	0.144	0.117	0.400	0.204
$t_{12}$	0.162	0.178	0.117	0.127	0.098	0.093
$t_{22}$	0.073	0.016	0.075	0.015	0.017	0.038
$r_0$	0.06	0.069	0.039	0.036	0.003	-0.015
$r_1$	-0.236	-0.261	-0.209	-0.234	-0.025	-0.209
$r_{11}$	0.016	-0.003	0.052	0.044	0.082	0.115
$r_{12}$	0.087	0.109	0.060	0.075	0.051	0.009
$r_2$	0.067	0.107	0.069	0.107	-0.169	0.107
$u_0$	-0.038	-0.054	-0.042	-0.061	0.057	-0.066
$u_1$	0.046	0.045	0.036	0.032	0.103	0.011
$u_2$	0.001	0.002	0.008	0.007	0.187	-0.013
$u_{11}$	0.266	0.325	0.272	0.329	-0.045	0.312
$u_{12}$	-0.176	-0.206	-0.172	-0.202	-0.141	-0.177
$u_{22}$	-0.15	-0.163	-0.150	-0.164	0.087	-0.132
$\lambda$	0.073	0.211	0.091	0.228	0.107	0.237

TABLE II. Parameters of three band tight-binding Hamiltonian. Here the lattice constant,  $a$ , is in units of Å, while all other parameters are in units of eV<sup>32</sup>.

Office of Science, US Department of Energy. Numerical simulations were performed using support by Grant No. DE-SC0007043 from the Materials Sciences and Engineering Division of the Office of the Basic Energy Sciences, Office of Science, US Department of Energy.

- 
- <sup>1</sup> Jonas Kiemle, Philipp Zimmermann, Alexander W. Holleitner, and Christoph Kastl, “Light-field and spin-orbit-driven currents in van der waals materials,” *Nanophotonics* **9**, 2693 (2020).
  - <sup>2</sup> Shawn Sederberg, Dmitry Zimin, Sabine Keiber, Florian Siegrist, Michael S. Wismer, Vladislav S. Yakovlev, Isabella Floss, Christoph Lemell, Joachim Burgdörfer, Martin Schultze, Ferenc Krausz, and Nicholas Karpowicz, “Attosecond optoelectronic field measurement in solids,” *Nature Communications* **11**, 430 (2020).
  - <sup>3</sup> A. Schiffrin, T. Paasch-Colberg, N. Karpowicz, V. Apalkov, D. Gerster, S. Muhlbrandt, M. Korbman, J. Reichert, M. Schultze, S. Holzner, J. V. Barth, R. Kienberger, R. Ernstorfer, V. S. Yakovlev, M. I. Stockman, and F. Krausz, “Optical-field-induced current in dielectrics,” *Nature* **493**, 70–74 (2012).
  - <sup>4</sup> Jie Li, Jian Lu, Andrew Chew, Seunghwoi Han, Jialin Li, Yi Wu, He Wang, Shambhu Ghimire, and Zenghu Chang, “Attosecond science based on high harmonic generation from gases and solids,” *Nature Communications* **11**, 2748 (2020).
  - <sup>5</sup> T. Paasch-Colberg, A. Schiffrin, N. Karpowicz, S. Kruchinin, Saglam Ozge, S. Keiber, O. Razskazovskaya, S. Muhlbrandt, A. Alnaser, M. Kubel, V. Apalkov, D. Gerster, J. Reichert, T. Wittmann, J. V. Barth, M. I. Stockman, R. Ernstorfer, V. S. Yakovlev, R. Kienberger, and F. Krausz, “Solid-state light-phase detector,” *Nat. Phot.* **8**, 214–218 (2014).
  - <sup>6</sup> V. Apalkov and M. I. Stockman, “Theory of dielectric nanofilms in strong ultrafast optical fields,” *Phys. Rev. B* **86**, 165118–1–13 (2012).
  - <sup>7</sup> Giulio Vampa, Jian Lu, Yong Sing You, Denitsa R Baykuseva, Mengxi Wu, Hanzhe Liu, Kenneth J Schafer, Mette B Gaarde, David A Reis, and Shambhu Ghimire, “Attosecond synchronization of extreme ultraviolet high harmonics from crystals,” *Journal of Physics B: Atomic, Molecular and Optical Physics* **53**, 144003 (2020).
  - <sup>8</sup> T. Higuchi, C. Heide, K. Ullmann, H. B. Weber, and P. Hommelhoff, “Light-field-driven currents in graphene,” *Nature* **550**, 224–228 (2017).
  - <sup>9</sup> Elisabeth Gruber, Richard A. Wilhelm, Rémi Pétuya, Valerie Smejkal, Roland Kozubek, Anke Hierzenberger, Bernhard C. Bayer, Iñigo Aldazabal, Andrey K. Kazansky, Florian Libisch, Arkady V. Krashennnikov, Marika Schleberger, Stefan Facsko, Andrei G. Borisov, Andrés Arnau, and Friedrich Aumayr, “Ultrafast electronic response of graphene to a strong and localized electric field,” *Nat. Commun.* **7**, 13948 (2016).
  - <sup>10</sup> S. A. Oliaei Motlagh, V. Apalkov, and M. I. Stockman, “Interaction of crystalline topological insulator with an ultrashort laser pulse,” *Phys. Rev. B* **95**, 085438–1–8 (2017).
  - <sup>11</sup> S. A. O. Motlagh, J. S. Wu, V. Apalkov, and M. I. Stockman, “Fundamentally fastest optical processes at the surface of a topological insulator,” *Phys. Rev. B* **98**, 125410–1–11 (2018).
  - <sup>12</sup> C. Heide, T. Higuchi, H. B. Weber, and P. Hommelhoff, “Coherent electron trajectory control in graphene,” *Phys. Rev. Lett.* **121**, 207401–1–5 (2018).
  - <sup>13</sup> Christian Heide, Tobias Boolakee, Takuya Higuchi, Heiko B Weber, and Peter Hommelhoff, “Interaction of carrier envelope phase-stable laser pulses with graphene: the transition from the weak-field to the strong-field regime,” *New J. Phys.* **21**, 045003 (2019).
  - <sup>14</sup> Dong Sun, Grant Aivazian, Aaron M. Jones, Jason S.



- Ross, Wang Yao, David Cobden, and Xiaodong Xu, “Ultrafast hot-carrier-dominated photocurrent in graphene,” *Nat. Nanotechnol.* **7**, 114 (2012).
- <sup>15</sup> Hiroki Mashiko, Yuta Chisuga, Ikufumi Katayama, Katsuya Oguri, Hiroyuki Masuda, Jun Takeda, and Hideki Gotoh, “Multi-petahertz electron interference in *cr:al2o3* solid-state material,” *Nat. Commun.* **9**, 1468 (2018).
  - <sup>16</sup> Hee Jun Shin, Van Luan Nguyen, Seong Chu Lim, and Joo-Hiuk Son, “Ultrafast nonlinear travel of hot carriers driven by high-field terahertz pulse,” *J. Phys. B: At. Mol. Opt. Phys.* **51**, 144003 (2018).
  - <sup>17</sup> Takuya Higuchi, Christian Heide, Konrad Ullmann, Heiko B. Weber, and Peter Hommelhoff, “Light-field-driven currents in graphene,” *Nature* **550**, 224–228 (2017).
  - <sup>18</sup> M. Trushin, A. Grupp, G. Soavi, A. Budweg, D. De Fazio, U. Sassi, A. Lombardo, A. C. Ferrari, W. Belzig, A. Leitenstorfer, and D. Brida, “Ultrafast pseudospin dynamics in graphene,” *Phys. Rev. B* **92**, 165429 (2015).
  - <sup>19</sup> S. A. Oliaei Motlagh, J.-S. Wu, V. Apalkov, and M. I. Stockman, “Femtosecond valley polarization and topological resonances in transition metal dichalcogenides,” *Phys. Rev. B* **98**, 081406(R)–1–6 (2018).
  - <sup>20</sup> D. Sun, J. W. Lai, J. C. Ma, Q. S. Wang, and J. Liu, “Review of ultrafast spectroscopy studies of valley carrier dynamics in two-dimensional semiconducting transition metal dichalcogenides,” *Chin. Phys. B* **26** (2017).
  - <sup>21</sup> Jun Zhang, Hao Ouyang, Xin Zheng, Jie You, Runze Chen, Tong Zhou, Yizhen Sui, Yu Liu, Xiang’ai Cheng, and Tian Jiang, “Ultrafast saturable absorption of *mos2* nanosheets under different pulse-width excitation conditions,” *Opt. Lett.* **43**, 243–246 (2018).
  - <sup>22</sup> Yong Sing You, Yanchun Yin, Yi Wu, Andrew Chew, Xiaoming Ren, Fengjiang Zhuang, Shima Gholam-Mirzaei, Michael Chini, Zenghu Chang, and Shambhu Ghimire, “High-harmonic generation in amorphous solids,” *Nat. Commun.* **8**, 724 (2017).
  - <sup>23</sup> H. Z. Liu, Y. L. Li, Y. S. You, S. Ghimire, T. F. Heinz, and D. A. Reis, “High-harmonic generation from an atomically thin semiconductor,” *Nat. Phys.* **13**, 262–266 (2017).
  - <sup>24</sup> A. Kaiser, B. Rethfeld, M. Vicanek, and G. Simon, “Microscopic processes in dielectrics under irradiation by sub-picosecond laser pulses,” *Phys. Rev. B* **61**, 11437–11450 (2000).
  - <sup>25</sup> H. G. Rosa, J. A. Castaneda, C. H. B. Cruz, L. A. Padilha, J. C. V. Gomes, E. A. T. de Souza, and H. L. Fragnito, “Controlled stacking of graphene monolayer saturable absorbers for ultrashort pulse generation in erbium-doped fiber lasers,” *Opt. Mater. Express* **7**, 2528–2537 (2017).
  - <sup>26</sup> S. Kumar, M. Anija, N. Kamaraju, K. S. Vasu, K. S. Subrahmanyam, A. K. Sood, and C. N. R. Rao, “Femtosecond carrier dynamics and saturable absorption in graphene suspensions,” *Appl. Phys. Lett.* **95** (2009).
  - <sup>27</sup> F. Gesuele, “Ultrafast hyperspectral transient absorption spectroscopy: Application to single layer graphene,” *Photonics* **6** (2019).
  - <sup>28</sup> S. Azar Oliaei Motlagh, Ahmal Jawad Zafar, Aranyo Mitra, Vadym Apalkov, and Mark I. Stockman, “Ultrafast strong-field absorption in gapped graphene,” *Phys. Rev. B* **101**, 165433 (2020).
  - <sup>29</sup> Q. H. Wang, K. Kalantar-Zadeh, A. Kis, J. N. Coleman, and M. S. Strano, “Electronics and optoelectronics of two-dimensional transition metal dichalcogenides,” *Nature Nanotechnology* **7**, 699–712 (2012).
  - <sup>30</sup> K. S. Novoselov, A. Mishchenko, A. Carvalho, and A. H. C. Neto, “2d materials and van der Waals heterostructures,” *Science* **353**, 461–1–11 (2016).
  - <sup>31</sup> D. Xiao, G. B. Liu, W. X. Feng, X. D. Xu, and W. Yao, “Coupled spin and valley physics in monolayers of *MoS2* and other group-VI dichalcogenides,” *Phys. Rev. Lett.* **108** (2012).
  - <sup>32</sup> G. B. Liu, W. Y. Shan, Y. G. Yao, W. Yao, and D. Xiao, “Three-band tight-binding model for monolayers of group-VIB transition metal dichalcogenides,” *Phys. Rev. B* **88**, 085433–1–10 (2013).
  - <sup>33</sup> Naoto Nagaosa, Jairo Sinova, Shigeki Onoda, A. H. MacDonald, and N. P. Ong, “Anomalous Hall effect,” *Reviews of Modern Physics* **82**, 1539–1592 (2010).
  - <sup>34</sup> S. A. Oliaei Motlagh, F. Nematollahi, V. Apalkov, and M. I. Stockman, “Topological resonance and single-optical-cycle valley polarization in gapped graphene,” *Phys. Rev. B* **100**, 115431 (2019).
  - <sup>35</sup> S. Y. Zhou, G. H. Gweon, A. V. Fedorov, P. N. First, W. A. de Heer, D. H. Lee, F. Guinea, A. H. Castro Neto, and A. Lanzara, “Substrate-induced bandgap opening in epitaxial graphene,” *Nat. Mater.* **6**, 770 (2007).
  - <sup>36</sup> M. S. Nevius, M. Conrad, F. Wang, A. Celis, M. N. Nair, A. Taleb-Ibrahimi, A. Tejada, and E. H. Conrad, “Semiconducting graphene from highly ordered substrate interactions,” *Phys. Rev. Lett.* **115**, 136802 (2015).
  - <sup>37</sup> S. Azar Oliaei Motlagh, Fatemeh Nematollahi, Aranyo Mitra, Ahmal Jawad Zafar, Vadym Apalkov, and Mark I. Stockman, “Ultrafast optical currents in gapped graphene,” *Journal of Physics: Condensed Matter* **32**, 065305 (2019).
  - <sup>38</sup> E. H. Hwang and S. Das Sarma, “Single-particle relaxation time versus transport scattering time in a two-dimensional graphene layer,” *Phys. Rev. B* **77**, 195412–1–6 (2008).
  - <sup>39</sup> M. Breusing, S. Kuehn, T. Winzer, E. Malic, F. Milde, N. Severin, J. P. Rabe, C. Ropers, A. Knorr, and T. Elsaesser, “Ultrafast nonequilibrium carrier dynamics in a single graphene layer,” *Phys. Rev. B* **83**, 153410 (2011).
  - <sup>40</sup> D. Brida, A. Tomadin, C. Manzoni, Y. J. Kim, A. Lombardo, S. Milana, R. R. Nair, K. S. Novoselov, A. C. Ferrari, G. Cerullo, and M. Polini, “Ultrafast collinear scattering and carrier multiplication in graphene,” *Nat Commun* **4**, 1987–1–9 (2013).
  - <sup>41</sup> I. Gierz, J. C. Petersen, M. Mitrano, C. Cacho, I. C. Turcu, E. Springate, A. Stohr, A. Kohler, U. Starke, and A. Cavalleri, “Snapshots of non-equilibrium Dirac carrier distributions in graphene,” *Nat. Mater.* **12**, 1119–24 (2013).
  - <sup>42</sup> Andrea Tomadin, Daniele Brida, Giulio Cerullo, Andrea C. Ferrari, and Marco Polini, “Nonequilibrium dynamics of photoexcited electrons in graphene: Collinear scattering, Auger processes, and the impact of screening,” *Phys. Rev. B* **88**, 035430 (2013).
  - <sup>43</sup> W. V. Houston, “Acceleration of electrons in a crystal lattice,” *Phys. Rev.* **57**, 184–186 (1940).
  - <sup>44</sup> F. Bloch, “Über die Quantenmechanik der Elektronen in Kristallgittern,” *Z. Phys. A* **52**, 555–600 (1929).
  - <sup>45</sup> F. Wilczek and A. Zee, “Appearance of gauge structure in simple dynamical systems,” *Phys. Rev. Lett.* **52**, 2111–2114 (1984).
  - <sup>46</sup> D. Xiao, M.-C. Chang, and Q. Niu, “Berry phase effects on electronic properties,” *Reviews of Modern Physics* **82**, 1959–2007 (2010).
  - <sup>47</sup> F. Yang and R. B. Liu, “Nonlinear optical response induced by non-Abelian Berry curvature in time-reversal-invariant

- insulators,” *Phys. Rev. B* **90**, 245205 (2014).
- <sup>48</sup> Guilmot Ernotte, T. J. Hammond, and Marco Taucer, “A gauge-invariant formulation of interband and intraband currents in solids,” *Phys. Rev. B* **98**, 235202 (2018).
- <sup>49</sup> H. K. Keldar, V. Apalkov, and M. I. Stockman, “Graphene in ultrafast and superstrong laser fields,” *Phys. Rev. B* **91**, 045439–1–8 (2015).
- <sup>50</sup> F. Nematollahi, S. A. O. Motlagh, V. Apalkov, and M. I. Stockman, “Weyl semimetals in ultrafast laser fields,” *Phys. Rev. B* **99**, 245409–1–9 (2019).
- <sup>51</sup> F. Nematollahi, V. Apalkov, and M. I. Stockman, “Phosphorene in ultrafast laser field,” *Phys. Rev. B* **97**, 035407–1–6 (2018).
- <sup>52</sup> Christian Heide, Tobias Boolakee, Takuya Higuchi, and Peter Hommelhoff, “Sub-cycle temporal evolution of light-induced electron dynamics in hexagonal 2d materials,” *Journal of Physics: Photonics* **2**, 024004 (2020).